Journal of Applied Physics

RESEARCH ARTICLE | MARCH 10 2025

Multi-contrast benchmarking of edge illumination Monte Carlo simulations using virtual gratings

Jonathan Sanctorum ; Jan Sijbers ; Jan De Beenhouwer

J. Appl. Phys. 137, 104904 (2025)
https://doi.org/10.1063/5.0244152

AIP Publishing

Journal of Applied Physics ARTICLE pubs.aip.org/aip/jap

Multi-contrast benchmarking of edge illumination Monte Carlo simulations using virtual gratings

Cite as: J. Appl. Phys. **137**, 104904 (2025); doi: 10.1063/5.0244152
Submitted: 16 October 2024 · Accepted: 13 February 2025 ·
Published Online: 10 March 2025

Jonathan Sanctorum,[1,2,a)] Jan Sijbers,[1,2] and Jan De Beenhouwer[1,2]

AFFILIATIONS

[1]imec-Vision Lab, Department of Physics, University of Antwerp, Antwerpen, Belgium
[2]DynXlab: Center for 4D Quantitative X-ray Imaging and Analysis, Antwerpen, Belgium

[a)]**Author to whom correspondence should be addressed:** jonathan.sanctorum@uantwerpen.be

ABSTRACT

In recent years, the complementary nature of multi-contrast imaging has increased the popularity of x-ray phase contrast imaging, including edge illumination. However, edge illumination system optimization most often relies on phase and transmission contrast only, without considering dark field contrast. Computer simulations are a widespread approach to design and optimize imaging systems, including the benchmarking of simulation results, i.e., the comparison to a reference value. Providing such a reference is, however, particularly challenging for the dark field signal. In this work, we present a practical method to directly estimate transmission, refraction, and dark field contrast reference values from simulated x-ray trajectories in Monte Carlo simulations. This allows an immediate comparison of the retrieved simulated contrasts to their respective references. We show how the generated reference values can be used effectively for benchmarking simulation results and discuss other potential applications of the presented approach.

I. INTRODUCTION

The increased accessibility of x-ray phase contrast imaging (XPCI) using compact laboratory systems has boosted its development in recent years,[1–5] resulting in various applications such as spectral imaging and material decomposition,[6–8] virtual histology,[9] and clinical dark field based imaging of lungs.[10] XPCI, or more specifically, differential phase contrast (DPC) imaging, is known for its capability to yield high contrast compared to conventional attenuation contrast (AC) in, e.g., soft tissue and polymer samples, making it a valuable tool for non-destructive testing and (bio) medical applications. Next to AC and DPC, dark field contrast (DFC) is a third contrast type that has been receiving increased interest in recent years due to its unique ability to provide information about unresolved microstructures.[11,12] Both DPC and DFC are related to the x-ray refractive index of the object, but as opposed to DPC, DFC results from refractive index fluctuations that cannot be resolved by the imaging system.[13] This results in a local increase in the angular spread of the x-ray beam,[14,15] referred to as angular broadening. Measurement of the DFC signal is traditionally performed with XPCI methods featuring optical components, such as analyzer based imaging (ABI),[16] grating-based interferometry (GBI),[11] edge illumination (EI),[12] beam tracking (BT),[17] single-grid imaging (SGI),[18] and speckle-based imaging (SBI).[19] More recently, however, DFC imaging has been demonstrated using propagation-based imaging (PBI) as well.[20,21]

Whereas GBI is arguably the most popular experimental configuration for DFC imaging, EI is another emerging DFC method suitable for lab-based setups.[4] Relying on two gratings, the EI DFC signal is extracted from the broadening of an intensity curve, generated by laterally shifting one grating with respect to the other.[22] In contrast to recent developments in GBI,[10,23–26] DFC is hardly ever considered when making design choices for multi-contrast EI systems. Indeed, most studies are predominantly oriented toward DPC, while assessment of DFC is minimal or even absent.[27–35] A rare exception is the work of Astolfo *et al.* concerning the design of a large field-of-view (FOV) EI system.[36,37] It has been shown that, compared to AC and DPC, DFC is significantly more sensitive to grating imperfections and misalignment[38] and is affected by polychromatic effects such as beam hardening, resulting from both the imaged object and partially transmitting grating bars.[15,39] Furthermore, it has been suggested that the choice of system and grating parameters could influence the

linearity of the measured DFC,[40] which is important for tomography applications.[41]

Optimization and design of EI setups often relies on computer simulations.[28,33,35,36,42,43] Benchmarking the simulated DFC signal originating from an arbitrary object is not trivial and is often omitted. Since the first observations of x-ray beam broadening due to microstructures,[44] there have been many efforts in modeling this effect and relating it to unresolved sample properties.[13,45–58] In practice, simulation models are often simplified to reduce simulation times, for example by condensing the dark field effect in a single (linear) material parameter or by imposing an *a priori* scattering distribution.[16,36,48,59,60] Another possible approach is to calibrate the linear model using experimental data,[36] but this quickly becomes unfeasible if there is a directional dependency in the signal due to the complicated sampling schemes involved in measuring directional DFC.[61,62] Among other methods, Monte Carlo (MC) simulators are commonly used for EI-XPCI simulations.[36,63–65] A balanced approach, avoiding a number of limiting assumptions such as isotropic distributions or linearity while keeping the simulation cost reasonable, is to explicitly model the microstructures in the simulation.[50,62,66] In such a MC simulation, angular broadening is generated by the combined effect of many refraction events. The retrieved DFC will depend on the characteristics of the simulated setup and contrast retrieval algorithm as well.[36,37] As such, in order to assess which parameters yield the most accurate result, the retrieved DFC must be benchmarked using a reference value.[59] In general, however, such a reference value is not readily available for comparison.

In this work, we demonstrate an approach to simultaneously simulate the retrieved contrasts (AC, DPC, and DFC) and corresponding reference values, allowing full multi-contrast benchmarking of MC simulation results. The presented method relies on the virtual grating approach, which was recently developed to reduce simulation times for large parameter studies.[65] We show how this method can be used for multi-contrast benchmarking of simulation results and briefly discuss both its limitations and other potential applications.

II. METHODS

A. Edge illumination

Figure 1 shows a schematic overview of an EI setup, including two absorbing gratings: one in front of the sample and one in front of the detector. The first grating is known as the sample mask and serves as a beam splitter, subdividing the incoming x-ray beam in several smaller beamlets. In a standard EI configuration, each beamlet corresponds to exactly one pixel column on the detector. The amount of illumination received by each pixel depends on the relative position between the sample mask and second grating, the detector mask. By shifting the sample mask along the x-direction in Fig. 1, the projected positions of the beamlets on the detector mask will shift accordingly. If the projected beamlet falls perfectly within the aperture of the detector mask, the measured intensity is maximal. Shifting away from this position to either side will gradually decrease the received illumination, until the beamlet is fully blocked by the grating bar, resulting in minimal illumination.

The detector pixel illumination as a function of the sample mask translation is referred to as the illumination curve (IC).[12] The IC, depicted in Fig. 1, can be used to retrieve three different contrasts. First, part of the incoming x rays will be absorbed by the object, reducing the total intensity in the beamlet and the area under the IC (AC). Second, refraction in the object will deflect the beamlet from its original path, shifting the IC (DPC). Finally, angular broadening due to unresolvable microstructures increases the IC width (DFC).

In practice, an EI experiment involves sampling the IC with a finite number of grating shifts, known as mask stepping. At least three IC positions are required to retrieve all three contrasts. Contrast retrieval is usually performed by fitting the sampled IC

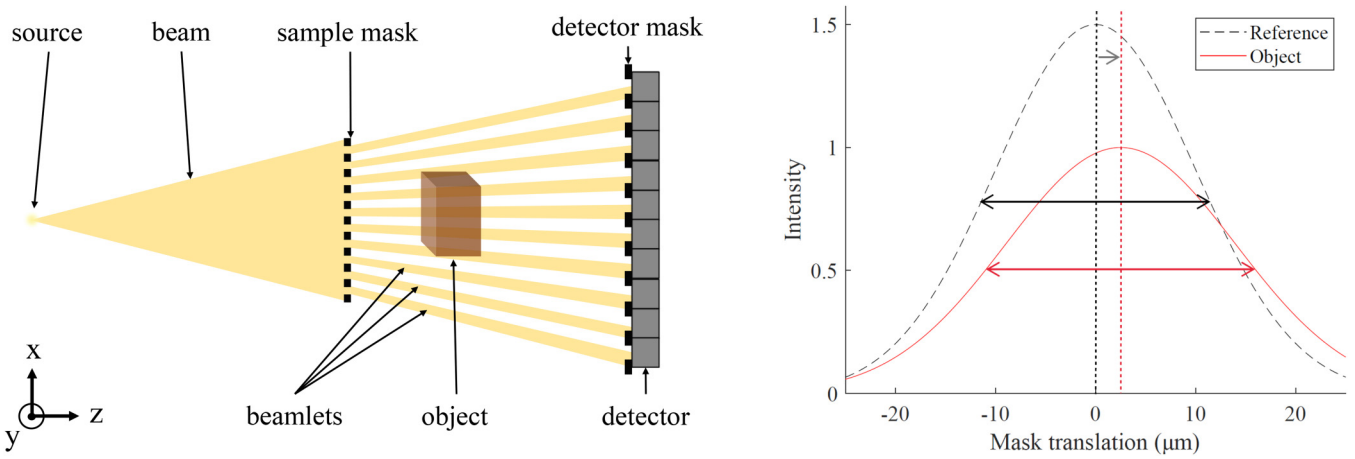

FIG. 1. Left: schematic overview of an EI system (not to scale). Right: illustration of an IC with and without sample. The arrows indicate the IC shift and broadening, which are linked to refraction and dark field, respectively.

with a Gaussian function in the sample mask plane

$$\mathrm{IC}(x_s) = \frac{a}{c\sqrt{2\pi}} \exp\left(-\frac{(x_s - b)^2}{2c^2}\right), \tag{1}$$

with a being the area under the IC, b being the position of the mean, and c^2 being the variance. As such, transmission, beamlet shift, and beamlet broadening in the sample mask coordinate system are given by

$$T = \frac{a_1}{a_0}, \tag{2}$$

$$\Delta b = b_1 - b_0, \tag{3}$$

$$\Delta c^2 = c_1^2 - c_0^2, \tag{4}$$

respectively, where the projection with the sample and corresponding flat field are denoted by indices 1 and 0, respectively. The AC can be computed from T as $-\ln T$, although this additional conversion step is omitted in this work. The local x-ray refraction angle α (DPC) can be calculated from Δb by accounting for the distance between sample and detector d_{OD} and the magnification M,[67]

$$\alpha = \frac{M}{d_{\mathrm{OD}}} \Delta b. \tag{5}$$

Here, it is assumed that the small angle approximation holds. Similarly,[36,41] the angular broadening σ^2 can be calculated from Δc^2,

$$\sigma^2 = \left(\frac{M}{\mathrm{d_{OD}}}\right)^2 \Delta c^2. \tag{6}$$

It should be noted that under certain circumstances, such as residual transmission through the grating bars, an offset might be present in the measured IC, which can be modeled by adding an offset parameter to the model in Eq. (1).[15,36,39] Similarly, overlap of neighboring beamlets can hamper the detection of weaker dark field signals, which can be compensated for by simultaneous fitting of neighboring curves.[68,69]

B. Monte Carlo simulations in GATE

The simulations in this work are performed with our previously developed in-house version of GATE, a versatile MC framework for computed tomography (CT), positron emission tomography (PET), and single-photon emission computed tomography (SPECT) simulations based on Geant4.[70–72] In our in-house version, EI-XPCI simulations rely on the implementation of x-ray refraction.[66] On top of the already implemented XPCI functionalities, a novel method to model the gratings was recently introduced, being the virtual grating (VG) approach.[65] In the VG approach, each grating in the simulation is replaced by a transparent volume at the exact same location. These volumes register the entrance and exit coordinates of intersecting photon trajectories, adding them to the ROOT output.[73] As a consequence, given that the intersection coordinates of all detected photons are known for both grating positions, the grating geometry can be defined post-simulation. This leads to significantly reduced simulation times if many grating geometries are to be tested for the same phantom, at the cost of an increased output size.[65]

C. Finding reference values using a virtual grating approach

Multi-contrast reference values are required for the benchmarking of EI simulations, meaning the reference T, α, and σ^2 are to be determined for each x-ray beamlet. Here, σ^2 is the increase in angular variance of photon directions within a single beamlet. The angular variance is a measure for the spread in photon directions relative to the average direction in the beamlet. This is illustrated in Fig. 2.

If a virtual grating volume is placed at the position of the sample mask in the simulation, and a second virtual grating volume is placed at the detector mask position, the direction vectors of the photon trajectories before and after interaction with the phantom can be retrieved. Indeed, if the intersection points with the front and back planes of the virtual grating volume are written as $\mathbf{r}_{\mathrm{in}} = (x_{\mathrm{in}}, y_{\mathrm{in}}, z_{\mathrm{in}})$ and $\mathbf{r}_{\mathrm{out}} = (x_{\mathrm{out}}, y_{\mathrm{out}}, z_{\mathrm{out}})$, then the direction vector for a given photon m is $\mathbf{r}_{\mathrm{d,m}} = (x_{\mathrm{d},m}, y_{\mathrm{d},m}, z_{\mathrm{d},m}) = \mathbf{r}_{\mathrm{out,m}} - \mathbf{r}_{\mathrm{in,m}}$. Due to the orientation of the grating bars (Fig. 1), the system will only be sensitive to refraction and broadening along the x-axis. Hence, to make a correct comparison with the contrast retrieval results, the reference σ^2 and α should be estimated from direction vectors projected along the y-axis. Assuming the projected direction vectors are normalized, the average projected direction of N_b photons in a beamlet $\mathbf{r}_{\mathrm{av}} = (x_{\mathrm{av}}, y_{\mathrm{av}}, z_{\mathrm{av}})$ can be written as

$$\mathbf{r}_{\mathrm{av}} = \left(\frac{1}{N_b}\sum_{m=1}^{N_b} x_{\mathrm{d},m},\ 0,\ \frac{1}{N_b}\sum_{m=1}^{N_b} z_{\mathrm{d},m}\right). \tag{7}$$

Subsequently, the individual angular deviations from all projected $\mathbf{r}_{\mathrm{d,m}}$ with respect to the average direction $\mathbf{r}_{\mathrm{av}}$ can be found through their respective dot products, yielding the angular variance around the mean direction

$$\sigma_{\mathrm{av}}^2 = \frac{1}{N_b}\sum_{m=1}^{N_b} \arccos\left(\mathbf{r}_{\mathrm{d,m}} \cdot \mathbf{r}_{\mathrm{av}}\right)^2. \tag{8}$$

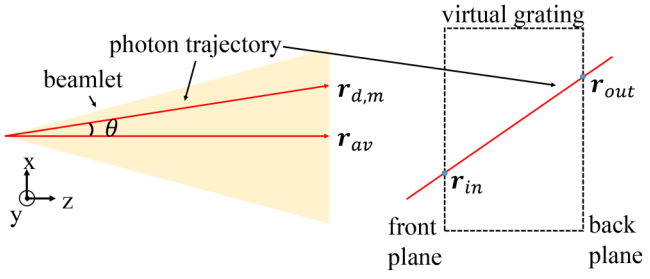

FIG. 2. Left: close up of a photon trajectory within a beamlet (not to scale). Right: intersection of a photon trajectory with the virtual grating volume.

If $\sigma^2_{av,0}$ denotes the result of Eq. (8) for the undistorted beamlet, then the reference for the angular broadening (and thus DFC) is given by

$$\sigma^2_R = \sigma^2_{av} - \sigma^2_{av,0}. \quad (9)$$

The change in average direction of the beamlet can be used to provide a reference for the refraction angle α_R,

$$\alpha_R = \arccos(\mathbf{r}_{av} \cdot \mathbf{r}_{av,0}), \quad (10)$$

yielding a reference value for DPC. In addition, due to the nature of the VG approach, the transmission reference T_R can be generated as well by omitting the gratings in the simulation, resulting in a conventional radiograph. For each measurement point (pixel), the reference values are extracted from the corresponding idealized beamlet, which is defined as the collection of photons passing through the aperture of an infinitesimally thin but perfectly absorbing mask. Hence, undesirable effects such as grating bar transmission and shadowing are eliminated, while still matching the mask stepping. This is a reasonable definition, since it leads to the exact set of photons that would contribute to an idealized EI measurement with perfect gratings. By design, the generated VG output can be used in parallel to generate simulated detector measurements, meaning that a single MC simulation suffices to simultaneously generate the reference and contrast retrieved values for an arbitrary number of grating geometries.[65] Subsequently, these profiles can be converted to T, α, and σ^2 through contrast retrieval.

To summarize, the proposed method uses the information stored by the VG approach to extract a complete set of reference values for all three contrasts, as well as mask stepping measurements. To differentiate between the contrast retrieval results (T, α, and σ^2) and the corresponding reference values, we will refer to the latter as T_R, α_R, and σ^2_R, respectively.

D. Geometrical optics model for EI simulations

A full description of x-ray phase effect generally requires wave optics modeling. Using GATE with x-ray refraction but without wavefront propagation, however, implies geometrical optics modeling. Although EI is an imaging method that can, in most cases, be modeled with geometrical optics, it is useful to briefly touch upon the geometrical optics approximation. In general, a distinction is made between three imaging regimes: the Fraunhofer regime, the Fresnel regime, and the geometrical optics regime. Although moving from one regime to another is a gradual change without clear boundaries, differentiation is possible through the Fresnel number N_F,

$$N_F = \frac{M(\Delta x_r)^2}{\lambda d_{OD}}, \quad (11)$$

where λ denotes the x-ray wavelength and Δx_r is the smallest resolvable transverse characteristic feature size.[74] The typically used condition for using the geometrical optics model, is that $N_F \gg 1$, with lower limit $N_F > 10$, demarcating the relevant imaging conditions. Smaller Fresnel numbers lead to the Fresnel ($N_F \approx 1$) and Fraunhofer ($N_F \ll 1$) regimes. An in-depth discussion with respect to aperture size and focal spot can be found in the work of Munro *et al.*[75,76]

III. EXPERIMENTS

A number of VG simulation experiments were performed in GATE to demonstrate the proposed method. The source-to-detector distance (SDD) of the simulated system was 1800 mm, with a 1.5 magnification factor for the sample mask, placed at distance of 1200 mm from the source. The detector mask was positioned at 5 mm in front of a line-detector, which consisted of 444 pixels with a size of 150 μm. X rays were generated from a polychromatic 40 kV source[77] (Fig. 3) with a Gaussian focal spot of 50 μm FWHM. Given the system dimensions and the spectrum having a weighted mean x-ray energy of 15.3 keV, Eq. (11) sets the geometrical optics limit for Δx_r at 18 μm. Since in EI, the aperture size determines a lower limit to the smallest resolvable features,[30] this means the aperture size should, in this case, be at least 18 μm. In total, 10^8 photons were generated at the source for every VG simulation. The phantoms were positioned between the two gratings, 30 mm from the sample mask. For each phantom, one VG simulation was performed, providing the required output for generating both the mask stepping results and reference values. To produce the mask stepping profiles, 15 mask steps were taken post-simulation for every grating geometry.[65] The sample mask aperture size was varied in steps of 5 μm from 20 to 40 μm, whereas the grating thickness for both gratings was varied from 150 to 350 μm in steps of 50 μm. The detector mask apertures scaled with the

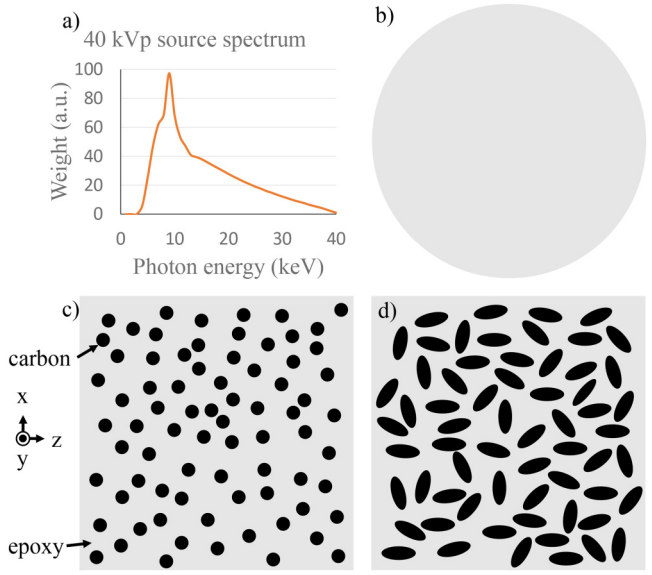

FIG. 3. (a) Spectrum of the simulated 40 kV x-ray source. Schematic view (not to scale) of (b) the simulated 10 mm epoxy cylinder, (c) the CFRP phantom with 10 μm symmetric fibers, and (d) the CFRP phantom with eccentric fibers (semi-axes of 12.5 and 5 μm).

sample mask apertures according to the magnification. This resulted in 25 different parameter combinations and 375 profiles in total for each phantom. For the mask stepping results, gold gratings were considered.

In total, three different phantoms were designed for the simulations. First, a 10 mm thick carbon fiber reinforced polymer (CFRP) phantom was used, consisting of cylindrical carbon fibers embedded in an epoxy matrix. The diameter of the fibers was set to 10 μm. To demonstrate the method on more arbitrarily shaped structures, the fibers were, in a second simulation, elongated to elliptical tubes with a long semi-axis of 12.5 μm and short semi-axis of 5 μm. The y-axis rotation of the eccentric fibers was randomly assigned, in order to avoid global directional dark field effects (Fig. 3). A Poisson disk sampling algorithm was used to determine the positions of the symmetric and eccentric fibers in the phantoms, where the longest axis of the eccentric fibers was used to define the minimal separation distance between sampling points. In total, 290 755 sampling points were generated for both phantoms. In addition to the microstructure phantoms, a homogeneous epoxy cylinder with 10 mm diameter was simulated. Finally, a simulation without phantom was performed. The imaging conditions were kept the same for all simulations.

GATE simulations were performed on a server with 16 Intel Xeon E5-2670 @ 2.60 GHz CPUs (dual core) and 64 GB RAM, using five cores in parallel for each simulation. The subsequent processing and analysis of the virtual grating simulation results was performed in MATLAB R2019a on a local machine with an NVIDIA GeForce GTX 1080 GPU, 6 Intel Core i7-6850K 3.60 GHz CPUs (dual core), and 64 GB RAM.

IV. RESULTS

The simulation times in GATE and the subsequent MATLAB processing times required to compute the mask stepping profiles are summarized in Table I. For GATE, the phantom complexity is the main factor determining the simulation time for a given number of photon trajectories. Since tracking of absorbed photons is stopped after absorption by the phantom, the average simulation time of the cylinder simulation is shorter compared to the average flat field simulation time. The processing times in MATLAB are mostly determined by the number of detected photons, given that the number of VG parameter variations is kept constant. The higher memory cost associated with an increasing number of photons, i.e., larger arrays, leads to longer computation times.

TABLE I. Monte Carlo simulation (GATE) and processing (MATLAB) times required to compute the mask stepping profiles for all experiments for each phantom described in Sec. III. All times are expressed in seconds, and the tabulated values are averages of the five parallel simulations.

	GATE	MATLAB
Cylinder	5 410 ± 20	6 940 ± 60
Symmetric fibers	10 390 ± 80	4 510 ± 30
Eccentric fibers	36 500 ± 400	4 270 ± 20
Flat field	6 480 ± 40	7 280 ± 20

A. Interpretation of α_R and σ_R^2

In Figs. 4–6, α_R and σ_R^2 profiles are plotted jointly with α and σ^2 profiles for the epoxy cylinder and the two fiber phantoms, respectively. In these plots, a distinction is made between type-1 and type-2 reference values.

The type-1 reference values require two simulations: one with and one without object in the beam path. When calculating σ_R^2 using Eq. (9), the simulation without object yields $\sigma_{av,0}^2$ and the simulation with object σ_{av}^2. In the type-2 reference plots, $\sigma_{av,0}^2$ and σ_{av}^2 both result from the simulation with object. However, $\sigma_{av,0}^2$ is calculated from the photon trajectories registered before interaction with the object and σ_{av}^2 from the same trajectories after interaction. Since by default only photons reaching the detector plane contribute to $\sigma_{av,0}^2$ and σ_{av}^2 in GATE, this implies that, for the type-2 case, $\sigma_{av,0}^2$ and σ_{av}^2 are extracted from the exact same set of simulated photons at different points in time. Hence, type-2 reference values are free from beam hardening effects. All previous considerations apply to type-1 and type-2 versions of α_R with respect to $\mathbf{r}_{av}$ and $\mathbf{r}_{av,0}$ in Eq. (10) as well.

Due to the definition of type-2 reference values, the corresponding type-2 plots for the epoxy cylinder in Fig. 4 show no fluctuations. Using a type-1 reference with a different set of simulated photons results in statistical fluctuations, visible in the type-1 plots. Furthermore, it can be seen that in the contrast retrieval plots the fluctuations become even more apparent due to the contrast retrieval procedure. The edge effects in the outer cylinder regions can be clearly seen in the reference plots but are washed out by the contrast retrieval.

It should be noted that all plots in Figs. 5 and 6 show fluctuations inside the CFRP phantom region, including the type-2 plots. Outside the object, however, the type-2 profiles are still flat. This indicates that these fluctuations are due to local spatial variations in the object microstructure, which is supported by the absence of these fluctuations in the type-2 profiles of the homogeneous cylinder. Since type-1 reference values are closer to actual EI measurements than type-2 reference values, type-1 will be used in the remainder of the work. Hence, unless stated otherwise, all reference values should be interpreted as type-1 reference values.

B. Benchmarking contrast retrieval results

In this section, the contrast retrieval results are benchmarked to the corresponding reference values. Assessment is performed in terms of the sum of squared errors (SSE) for α and accuracy A for T and σ^2, defined as the relative difference between the spatially averaged values

$$A_{\sigma^2} = \frac{\langle \sigma^2 \rangle_{ROI} - \langle \sigma_R^2 \rangle_{ROI}}{|\langle \sigma_R^2 \rangle_{ROI}|}, \tag{12}$$

where $\langle \cdot \rangle_{ROI}$ denotes the spatial average in the object region of interest (ROI), which is defined as the image region containing only the object pixels and no background pixels. An equivalent expression is used for A_T. The results of Eq. (12) are summarized in heat maps shown in Figs. 7 and 8. Each value corresponds to a specific grating geometry, defined by its aperture size and grating thickness. This is indicated on the horizontal and vertical axis,

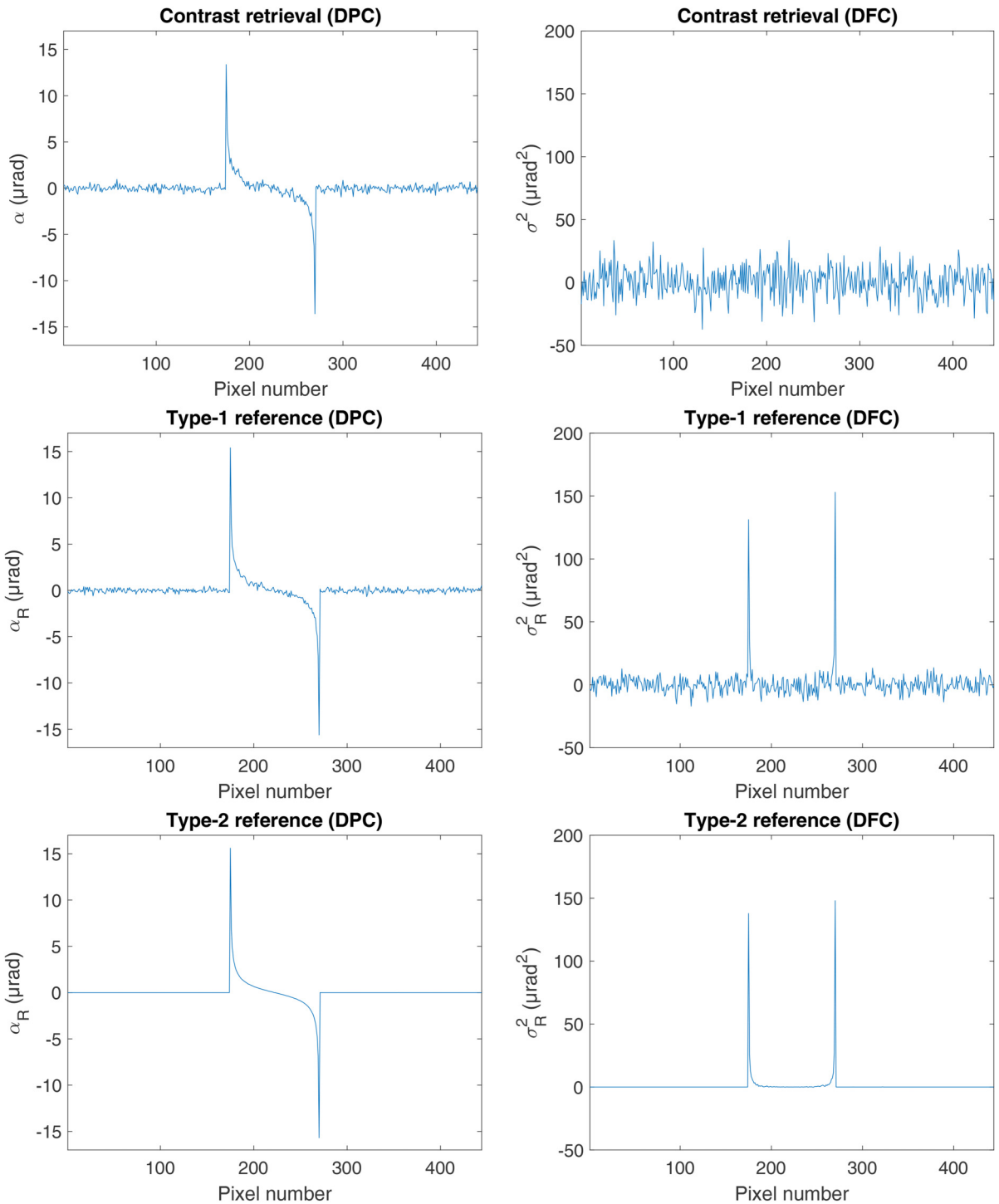

FIG. 4. α (refraction), α_R (refraction reference), σ^2 (dark field), and σ_R^2 (dark field reference) profiles resulting from the VG simulation with the single epoxy cylinder. The aperture size was set to 20 μm. For the contrast retrieval results, the grating thickness was set to 200 μm. The cylinder edges are clearly represented in all profiles except for the DFC retrieved from the IC profiles. The contrast retrieval results show the strongest signal fluctuations, whereas the type-2 references are, by definition, completely free of such fluctuations.

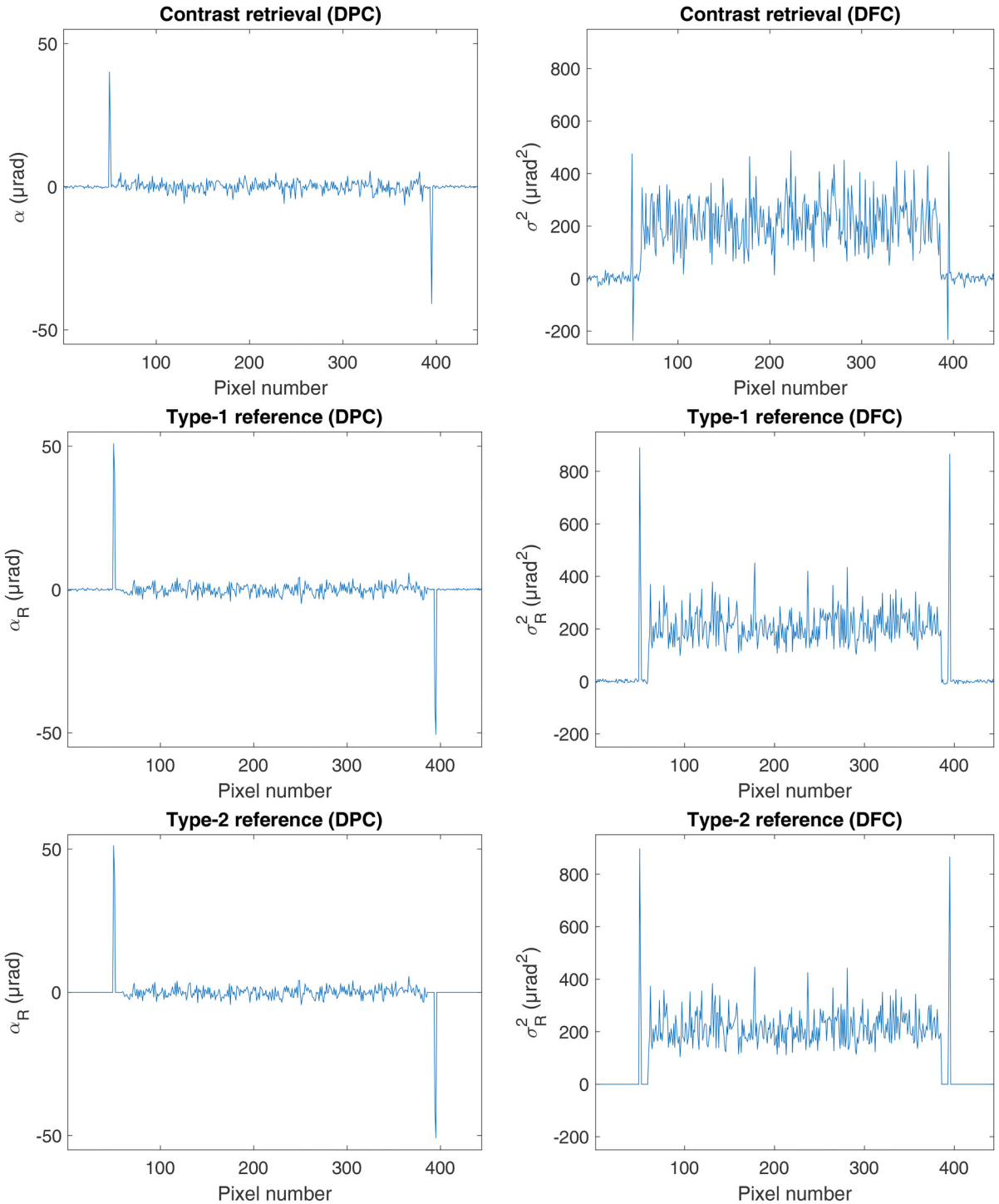

FIG. 5. α (refraction), α_R (refraction reference), σ^2 (dark field), and σ_R^2 (dark field reference) profiles resulting from the VG simulation with the 10 μm symmetric fiber CFRP phantom. The aperture size was set to 20 μm. For the contrast retrieval results, the grating thickness was set to 200 μm. The CFRP edges are clearly represented in all profiles. Here, the fluctuations only disappear in the background of the type-2 references and not within the CFRP region, indicating that they are in this case related to the presence of microstructures.

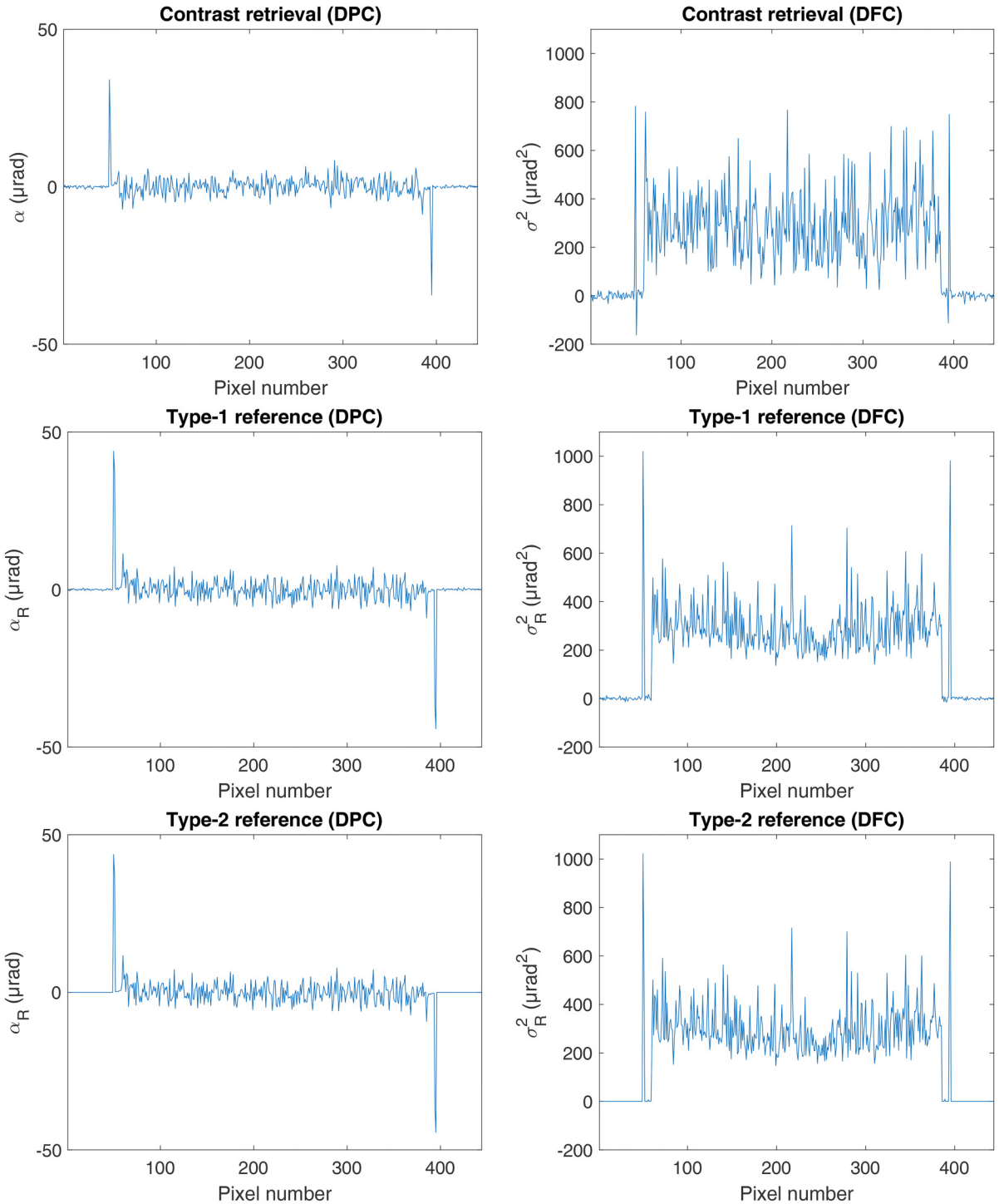

FIG. 6. α (refraction), α_R (refraction reference), σ^2 (dark field), and σ_R^2 (dark field reference) profiles resulting from the VG simulation with the eccentric fiber CFRP phantom. The aperture size was set to 20 μm. For the contrast retrieval results, the grating thickness was set to 200 μm. The average DFC is clearly higher compared to the CFRP with symmetric fibers. In addition, the signal fluctuations within the CFRP are visibly stronger for both DPC and DFC compared to the symmetric fibers, indicating that the magnitude of the fluctuations is related to the microstructure properties.

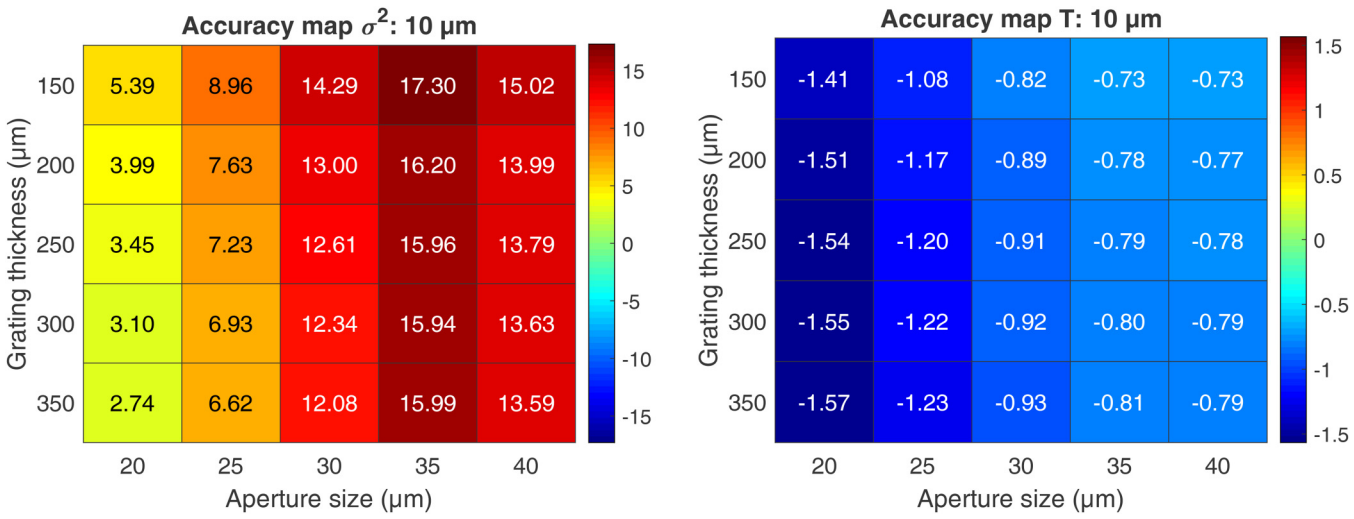

FIG. 7. Accuracy heat maps of σ^2 (dark field) and T (transmission) for the CFRP phantom with symmetric 10 μm fibers. Tabulated values are expressed in % and represent the accuracy as defined in Eq. (12) for different combinations of grating parameters (thickness and aperture size). Values represented by red cells indicate an overestimation of the respective reference values, whereas blue indicates an underestimation. Green cells represent the most optimal grating parameters. Smaller apertures tend to give more accurate σ^2 estimates, whereas larger apertures yield more accurate T values.

respectively. The color map is chosen such that a green value corresponds to optimal accuracy, i.e., A close to 0, whereas darker red and blue values indicate stronger deviations. Some degree of saturation in the color scale is tolerated for higher values, to ensure sufficient contrast in the heat map for lower, more optimal values. Tables summarizing the T and σ^2 values used to generate the accuracy heat maps can be found in the supplementary material.

It can be seen from Fig. 7 that smaller apertures tend to give more accurate σ^2 results, which is in line with expectations and the higher DPC sensitivity generally associated with smaller apertures.

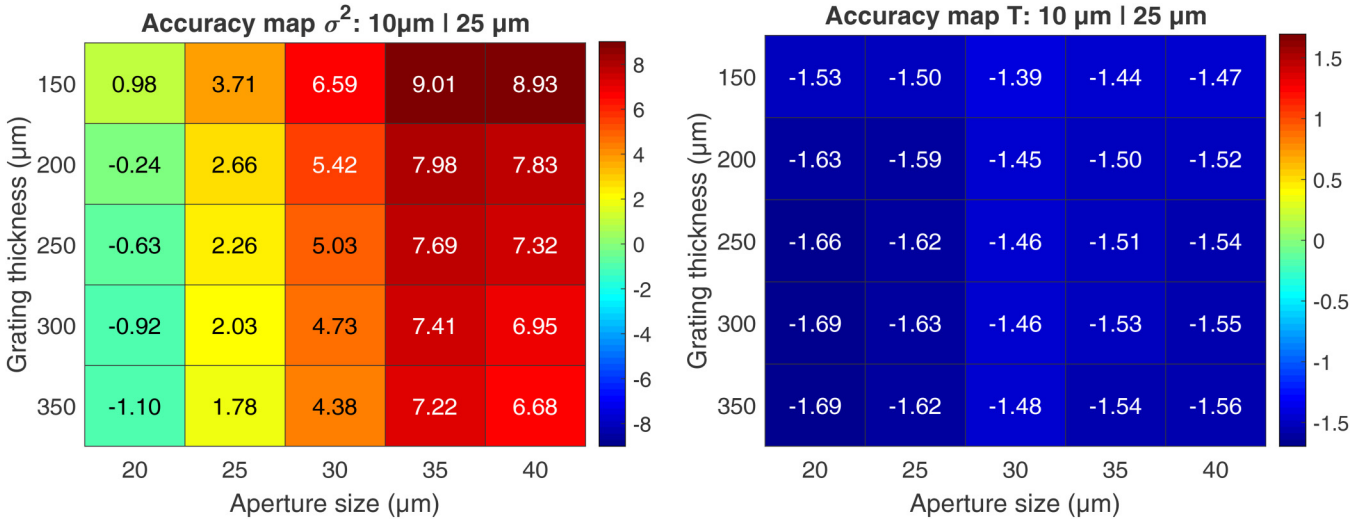

FIG. 8. Accuracy heat maps of σ^2 (dark field) and T (transmission) for the eccentric fiber phantom (10/25 axis ratio). Tabulated values are expressed in % and represent the accuracy as defined in Eq. (12) for different combinations of grating parameters (thickness and aperture size). Values represented by red cells indicate an overestimation of the respective reference values, whereas blue indicates an underestimation. Green cells represent the most optimal grating parameters. The most accurate σ^2 estimate is found for the 20 μm aperture with 200 μm thickness, whereas no clear trend is visible for T values of this phantom.

A similar result is found from the eccentric fibers in Fig. 8, where again the 20 μm aperture is more favorable compared to other aperture sizes. In general, the effect of the grating thickness seems to be more subtle than the effect of the aperture size. The heat maps show a gradually decreasing trend for increasing grating thickness, indicating a lowering average σ^2 compared to the σ_R^2 (see the supplementary material). Differences are, however, small compared to the differences for varying aperture sizes. It should be noted that shadowing is a problem affecting all contrasts for setups with larger cone angles and thicker gratings. Some shadowing is present in the results shown here as well, but only limited for most grating configurations due to the relatively small cone angle in the simulated geometry (2.1°).

Judging from the accuracy maps for T, smaller apertures tend to give a more profound underestimation of T. Differences are, however, small, especially in Fig. 8. The slightly decreasing trend observed for A_{σ^2} with increasing grating thickness is present for A_T as well.

The results of the SSE between α and α_R are summarized in a heat map shown in Fig. 9. The color map, chosen to visualize the SSE, shows darker red for a lower SSE and lighter yellow for a higher SSE. It can be seen that the 40 μm apertures result in the highest SSE, whereas the lowest SSE is found for the 25 μm aperture. The influence of the grating thickness on the SSE appears to be negligible, with a consistently decreasing SSE for thicker gratings only visible with aperture sizes of 25, 35, and 40 μm. The negligible SSE variation within columns indicates that the effect of shadowing is small for the considered system geometry. The overall SSE is, however, clearly higher in the last column.

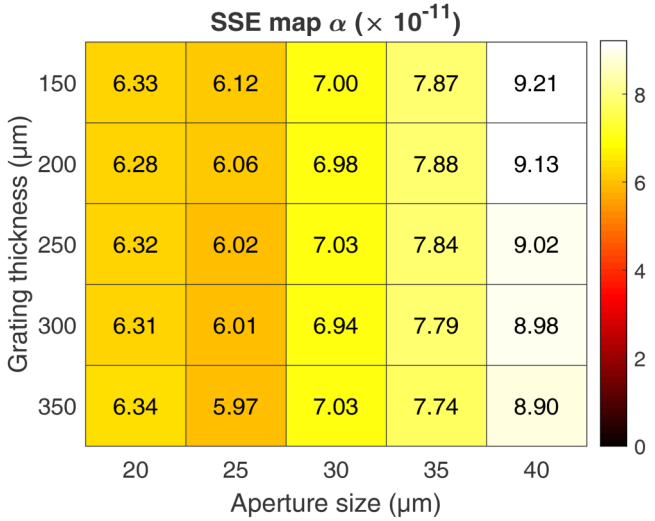

FIG. 9. SSE (sum of squared errors) heat map of α (refraction) for the single cylinder simulation, showing different combinations of aperture size and grating thickness. Darker red cells indicate lower, more optimal refraction estimates, whereas lighter yellow cells indicate larger deviations from the reference values. Smaller apertures yield more accurate refraction estimates, whereas the grating thickness has only limited influence.

V. DISCUSSION

The results shown in Sec. IV A illustrate that the most suitable definition for the reference type is problem-specific. Indeed, although type-1 reference values were chosen here to account for the most relevant physical interactions of x rays in the phantom, other arguments may lead to different choices. If beam hardening effects are to be removed from the reference, type-2 reference values gain interest. Choosing a type-2 reference does not avoid a change in effective spectrum, but by design absorbed photons do not contribute to the reference. Given that the energy of every photon is stored in the VG output, a more dedicated approach could be to carefully select a subset of photons from the VG output, in order to reconstruct the original spectrum. Although this avoids a change in effective spectrum, the significant loss of photons can affect the reference estimates.

Furthermore, the type-2 reference profiles plotted in Figs. 5 and 6 reveal that the presence of microstructures leads to fluctuations in α and σ^2 that cannot be attributed to photon statistics or the contrast retrieval procedure. This implies that these fluctuations result from intrinsic phantom properties such as local spatial variations in fiber concentration. It should be noted that such spatial signal fluctuations have received attention in recent experimental work as well,[78,79] where the standard deviation of α is treated as an alternative contrast type. The method presented in this work allows us to separate the intrinsic spatial fluctuations from other contributions such as photon statistics and contrast retrieval algorithms. The proposed method, therefore, seems well-suited to provide additional insight into how these fluctuations are related to specific microstructure properties, especially since this effect is mostly of interest for larger microstructures.

The accuracy and SSE maps shown in Figs. 7–9, provide a direct comparison of different grating designs for use in EI experiments based on all three contrast types. Figure 7 shows a slow but steady increase in A_T for increasing aperture size. Given that T_R is estimated from fully illuminated pixels, it is indeed to be expected that A_T improves when the effective pixel area illuminated by the beamlet approaches the full pixel size. This trend is less apparent in Fig. 8, where the A_T values show a more constant behavior. It is expected that this is due to the stronger beamlet broadening associated with the eccentric fiber phantom. Given that the size and shape of the fibers were different in both phantoms for the same total number of fibers, different packing densities are obtained. For the symmetric fibers, the packing density was found to be 7%, whereas for the eccentric fibers this was 17%, i.e., approximately 2.5 times higher. This difference is reflected by the corresponding average and standard deviation of the dark field (σ_R^2), which are consistently higher for the eccentric fiber phantom (see supplementary material). Differences in σ_R^2 between apertures are likely due to a change in number of photons and the effectively illuminated sample area. A possible alternative strategy could be to take the full period into account, although this implies that the set of trajectories used for the reference will no longer spatially match that of the contrast retrieval results. In addition to the examples presented in this work, the method is perfectly suited to test contrast retrieval methods, as its primary goal is to assess if information is extracted correctly from the simulation.

In Sec. III, Eq. (11) was used to find a lower limit on Δx_r for the validity of the geometrical optics model. It should be noted that this limit is indeed system dependent. A shorter system ($d_{OD} \downarrow$) would, for example, result in a smaller Δx_r value. Although for the 10 μm fiber case, the microstructure size lies below the estimated limit, the associated diffraction effects would not be resolvable with the modeled aperture and pixel sizes. If smaller apertures are of interest, wave optics simulations should be considered. Alternatively, the geometrical optics model could be extended through the geometrical theory of diffraction.[80] This would, however, result in a significantly increased computational cost. Hence, the current scope of our work is limited to systems for which the geometrical optics approach is a reasonable approximation. It should be noted that the weighted mean energy of the spectrum was used to determine the Δx_r limit. In practice, however, the majority of x rays that are not absorbed by the object and, therefore, contribute to the measurement, will have higher energies. The associated shorter wavelengths imply a lower effective Δx_r limit for these x rays.

A practical limit of the presented method is the fact that the VG approach tends to produce rather large output files for larger simulations.[33] If large simulations are required for a specific problem (e.g., 3D CT studies), the size of the output files could reach challenging proportions. A possible way to reduce the required output size would be to develop a dedicated VG output format storing only minimal amount of data. Standard ROOT output files store information that is not used in VG applications. However, data storage problems are not expected to become a limiting factor in the majority of cases.

VI. CONCLUSION

A method was presented to simultaneously simulate EI measurement data and corresponding T, α, and σ^2 reference values for multi-contrast benchmarking of EI simulations. The example cases presented in this work demonstrate how benchmarking can be performed without the need for additional simulations. Although GATE was used for our simulations, the method can be incorporated in any MC toolbox. Given the increasing interest in multi-contrast imaging, it is expected that the proposed method will prove to be useful for the optimization of future EI systems. In addition, we see a broader potential toward investigating the recently described "standard deviation of refraction contrast" attributed to mainly larger microstructures.

SUPPLEMENTARY MATERIAL

Data tables underlying the results presented in Figs. 7 and 8 are available in the supplementary material.

ACKNOWLEDGMENTS

The research presented in this work was financially supported by the Research Foundation—Flanders (FWO) through Grant Nos. S003421N (FoodPhase), G094320N, and G090020N.

AUTHOR DECLARATIONS

Conflict of Interest

The authors have no conflicts to disclose.

Author Contributions

Jonathan Sanctorum: Conceptualization (lead); Formal analysis (lead); Methodology (lead); Software (lead); Validation (lead); Visualization (lead); Writing – original draft (lead); Writing – review & editing (equal). **Jan Sijbers:** Conceptualization (supporting); Funding acquisition (equal); Methodology (supporting); Resources (lead); Supervision (equal); Writing – review & editing (equal). **Jan De Beenhouwer:** Conceptualization (supporting); Funding acquisition (equal); Methodology (supporting); Software (supporting); Supervision (equal); Writing – review & editing (equal).

DATA AVAILABILITY

The data that support the findings of this study are available from the corresponding author upon reasonable request.

REFERENCES

[1]M. Endrizzi, "X-ray phase-contrast imaging," Nucl. Instrum. Methods Phys. Res., Sect. A **878**, 88–98 (2018).
[2]A. Bravin, P. Coan, and P. Suortti, "X-ray phase-contrast imaging: From pre-clinical applications towards clinics," Phys. Med. Biol. **58**, R1–R35 (2013).
[3]A. Momose, "X-ray phase imaging reaching clinical uses," Phys. Med. **79**, 93–102 (2020).
[4]A. Olivo, "Edge-illumination x-ray phase-contrast imaging," J. Phys.: Condens. Matter **33**, 363002 (2021).
[5]L. Quenot, S. Bohic, and E. Brun, "X-ray phase contrast imaging from synchrotron to conventional sources: A review of the existing techniques for biological applications," Appl. Sci. **12**, 9539 (2022).
[6]X. Ji, R. Zhang, K. Li, and G.-H. Chen, "Dual energy differential phase contrast CT (DE-DPC-CT) imaging," IEEE Trans. Med. Imaging **39**, 3278–3289 (2020).
[7]E.-M. Braig, D. Pfeiffer, M. Willner, T. Sellerer, K. Taphorn, C. Petrich, J. Scholz, L. Petzold, L. Birnbacher, M. Dierolf, F. Pfeiffer, and J. Herzen, "Single spectrum three-material decomposition with grating-based x-ray phase-contrast CT," Phys. Med. Biol. **65**, 185011 (2020).
[8]L. Brombal, F. Arfelli, F. Brun, V. Di Trapani, M. Endrizzi, R. H. Menk, P. Perion, L. Rigon, M. Saccomano, G. Tromba, and A. Olivo, "Edge-illumination spectral phase-contrast tomography," Phys. Med. Biol. **69**, 075027 (2024).
[9]L. Massimi, T. Suaris, C. K. Hagen, M. Endrizzi, P. R. T. Munro, G. Havariyoun, P. M. S. Hawker, B. Smit, A. Astolfo, O. J. Larkin, R. M. Waltham, Z. Shah, S. W. Duffy, R. L. Nelan, A. Peel, J. L. Jones, I. G. Haig, D. Bate, and A. Olivo, "Volumetric high-resolution x-ray phase-contrast virtual histology of breast specimens with a compact laboratory system," IEEE Trans. Med. Imaging **41**, 1188–1195 (2022).
[10]T. Urban, F. T. Gassert, M. Frank, K. Willer, W. Noichl, P. Buchberger, R. C. Schick, T. Koehler, J. H. Bodden, A. A. Fingerle, A. P. Sauter, M. R. Makowski, F. Pfeiffer, and D. Pfeiffer, "Qualitative and quantitative assessment of emphysema using dark-field chest radiography," Radiology **303**, 119–127 (2022).
[11]F. Pfeiffer, M. Bech, O. Bunk, P. Kraft, E. F. Eikenberry, C. Brönnimann, C. Grünzweig, and C. David, "Hard-x-ray dark-field imaging using a grating interferometer," Nat. Mater. **7**, 134–137 (2008).

[12]M. Endrizzi, P. C. Diemoz, T. P. Millard, J. Louise Jones, R. D. Speller, I. K. Robinson, and A. Olivo, "Hard x-ray dark-field imaging with incoherent sample illumination," Appl. Phys. Lett. **104**, 024106 (2014).
[13]S. K. Lynch, V. Pai, J. Auxier, A. F. Stein, E. E. Bennett, C. K. Kemble, X. Xiao, W.-K. Lee, N. Y. Morgan, and H. H. Wen, "Interpretation of dark-field contrast and particle-size selectivity in grating interferometers," Appl. Opt. **50**, 4310–4319 (2011).
[14]M. Bech, T. Jensen, O. Bunk, T. Donath, C. David, T. Weitkamp, G. Le Duc, A. Bravin, P. Cloetens, and F. Pfeiffer, "Advanced contrast modalities for x-ray radiology: Phase-contrast and dark-field imaging using a grating interferometer," Z. Med. Phys. **20**, 7–16 (2010).
[15]M. Endrizzi and A. Olivo, "Absorption, refraction and scattering retrieval with an edge-illumination-based imaging setup," J. Phys. D: Appl. Phys. **47**, 505102 (2014).
[16]L. Rigon, F. Arfelli, and R.-H. Menk, "Three-image diffraction enhanced imaging algorithm to extract absorption, refraction, and ultrasmall-angle scattering," Appl. Phys. Lett. **90**, 114102 (2007).
[17]F. A. Vittoria, M. Endrizzi, P. C. Diemoz, U. H. Wagner, C. Rau, I. K. Robinson, and A. Olivo, "Virtual edge illumination and one dimensional beam tracking for absorption, refraction, and scattering retrieval," Appl. Phys. Lett. **104**, 134102 (2014).
[18]H. H. Wen, E. E. Bennett, R. Kopace, A. F. Stein, and V. Pai, "Single-shot x-ray differential phase-contrast and diffraction imaging using two-dimensional transmission gratings," Opt. Lett. **35**, 1932–1934 (2010).
[19]I. Zanette, T. Zhou, A. Burvall, U. Lundström, D. H. Larsson, M. Zdora, P. Thibault, F. Pfeiffer, and H. M. Hertz, "Speckle-based x-ray phase-contrast and dark-field imaging with a laboratory source," Phys. Rev. Lett. **112**, 253903 (2014).
[20]T. E. Gureyev, D. M. Paganin, B. Arhatari, S. T. Taba, S. Lewis, P. C. Brennan, and H. M. Quiney, "Dark-field signal extraction in propagation-based phase-contrast imaging," Phys. Med. Biol. **65**, 215029 (2020).
[21]T. A. Leatham, D. M. Paganin, and K. S. Morgan, "X-ray dark-field and phase retrieval without optics, via the Fokker–Planck equation," IEEE Trans. Med. Imaging **42**, 1681–1695 (2023).
[22]N. Matsunaga, K. Yano, M. Endrizzi, and A. Olivo, "Detection of individual sub-pixel features in edge-illumination x-ray phase contrast imaging by means of the dark-field channel," J. Phys. D: Appl. Phys. **53**, 095401 (2020).
[23]A. Yan, X. Wu, and H. Liu, "Predicting fringe visibility in dual-phase grating interferometry with polychromatic x-ray sources," J. X-ray Sci. Technol. **28**, 1055–1067 (2020).
[24]A. P. Sauter, J. Andrejewski, M. Frank, K. Willer, J. Herzen, F. Meurer, A. A. Fingerle, M. R. Makowski, F. Pfeiffer, and D. Pfeiffer, "Correlation of image quality parameters with tube voltage in x-ray dark-field chest radiography: A phantom study," Sci. Rep. **11**, 14130 (2021).
[25]C. Organista, M. Kagias, R. Tang, Z. Shi, K. Jefimovs, M. N. Boone, and M. Stampanoni, "Optimization of the visibility of a tunable dual-phase x-ray grating interferometer," Opt. Contin. **2**, 232–248 (2023).
[26]S. Spindler, D. Etter, M. Rawlik, M. Polikarpov, L. Romano, Z. Shi, K. Jefimovs, Z. Wang, and M. Stampanoni, "The choice of an autocorrelation length in dark-field lung imaging," Sci. Rep. **13**, 2731 (2023).
[27]A. Olivo and R. Speller, "Modelling of a novel x-ray phase contrast imaging technique based on coded apertures," Phys. Med. Biol. **52**, 6555–6573 (2007).
[28]A. Olivo, K. Ignatyev, P. Munro, and R. Speller, "Design and realization of a coded-aperture based x-ray phase contrast imaging for homeland security applications," Nucl. Instrum. Methods Phys. Res., Ser. A **610**, 604–614 (2009).
[29]A. Olivo, S. Gkoumas, M. Endrizzi, C. K. Hagen, M. B. Szafraniec, P. C. Diemoz, P. R. T. Munro, K. Ignatyev, B. Johnson, J. A. Horrocks, S. J. Vinnicombe, J. L. Jones, and R. D. Speller, "Low-dose phase contrast mammography with conventional x-ray sources," Med. Phys. **40**, 090701 (2013).
[30]P. Diemoz, M. Endrizzi, C. Hagen, T. Millard, F. Vittoria, and A. Olivo, "Angular sensitivity and spatial resolution in edge illumination x-ray phase-contrast imaging," Nucl. Instrum. Methods Phys. Res., Ser. A **784**, 538–541 (2015).
[31]G. Havariyoun, F. A. Vittoria, C. K. Hagen, D. Basta, G. K. Kallon, M. Endrizzi, L. Massimi, P. Munro, S. Hawker, B. Smit, A. Astolfo, O. J. Larkin, R. M. Waltham, Z. Shah, S. W. Duffy, R. L. Nelan, A. Peel, T. Suaris, J. L. Jones, I. G. Haig, D. Bate, and A. Olivo, "A compact system for intraoperative specimen imaging based on edge illumination x-ray phase contrast," Phys. Med. Biol. **64**, 235005 (2019).
[32]G. K. Kallon, F. A. Vittoria, I. Buchanan, M. Endrizzi, and A. Olivo, "An experimental approach to optimising refraction sensitivity for lab-based edge illumination phase contrast set-ups," J. Phys. D: Appl. Phys. **53**, 195404 (2020).
[33]J. Sanctorum, N. Six, J. Sijbers, and J. De Beenhouwer, "Augmenting a conventional x-ray scanner with edge illumination-based phase contrast imaging: How to design the gratings," Proc. SPIE **12242**, 1224218 (2022).
[34]L. Brombal, F. Arfelli, R. H. Menk, L. Rigon, and F. Brun, "PEPI lab: A flexible compact multi-modal setup for x-ray phase-contrast and spectral imaging," Sci. Rep. **13**, 4206 (2023).
[35]P.-J. Vanthienen, J. Sanctorum, B. Huyge, N. Six, J. Sijbers, and J. De Beenhouwer, "Grating designs for cone beam edge illumination x-ray phase contrast imaging: A simulation study," Opt. Express **31**, 28051–28064 (2023).
[36]A. Astolfo, M. Endrizzi, G. Kallon, T. P. Millard, F. A. Vittoria, and A. Olivo, "A first investigation of accuracy, precision and sensitivity of phase-based x-ray dark-field imaging," J. Phys. D: Appl. Phys. **49**, 485501 (2016).
[37]A. Astolfo, M. Endrizzi, F. A. Vittoria, P. C. Diemoz, B. Price, I. Haig, and A. Olivo, "Large field of view, fast and low dose multimodal phase-contrast imaging at high x-ray energy," Sci. Rep. **7**, 2187 (2017).
[38]M. Endrizzi, D. Basta, and A. Olivo, "Laboratory-based x-ray phase-contrast imaging with misaligned optical elements," Appl. Phys. Lett. **107**, 124103 (2015).
[39]F. A. Vittoria, G. K. N. Kallon, D. Basta, P. C. Diemoz, I. K. Robinson, A. Olivo, and M. Endrizzi, "Beam tracking approach for single–shot retrieval of absorption, refraction, and dark–field signals with laboratory x-ray sources," Appl. Phys. Lett. **106**, 224102 (2015).
[40]A. Astolfo, I. Buchanan, T. Partridge, G. K. Kallon, C. K. Hagen, P. R. T. Munro, M. Endrizzi, D. Bate, and A. Olivo, "The effect of a variable focal spot size on the contrast channels retrieved in edge-illumination X-ray phase contrast imaging," Sci. Rep. **12**, 3354 (2022).
[41]A. Doherty, S. Savvidis, C. Navarrete-León, M. F. Gerli, A. Olivo, and M. Endrizzi, "Edge-illumination x-ray dark-field tomography," Phys. Rev. Appl. **19**, 054042 (2023).
[42]F. A. Vittoria, P. C. Diemoz, M. Endrizzi, L. Rigon, F. C. Lopez, D. Dreossi, P. R. T. Munro, and A. Olivo, "Strategies for efficient and fast wave optics simulation of coded-aperture and other x-ray phase-contrast imaging methods," Appl. Opt. **52**, 6940–6947 (2013).
[43]I. Buchanan, G. Kallon, T. Beckenbach, J. Schulz, M. Endrizzi, and A. Olivo, "Effective modeling of high-energy laboratory-based x-ray phase contrast imaging utilizing absorption masks or gratings," J. Appl. Phys. **128**, 214503 (2020).
[44]C. M. Slack, "The refraction of x-rays in prisms of various materials," Phys. Rev. **27**, 691–695 (1926).
[45]R. von Nardroff, "Refraction of x-rays by small particles," Phys. Rev. **28**, 240–246 (1926).
[46]G. Khelashvili, J. G. Brankov, D. Chapman, M. A. Anastasio, Y. Yang, Z. Zhong, and M. N. Wernick, "A physical model of multiple-image radiography," Phys. Med. Biol. **51**, 221–236 (2006).
[47]W. Yashiro, Y. Terui, K. Kawabata, and A. Momose, "On the origin of visibility contrast in x-ray Talbot interferometry," Opt. Express **18**, 16890–16901 (2010).
[48]M. Bech, O. Bunk, T. Donath, R. Feidenhans'l, C. David, and F. Pfeiffer, "Quantitative x-ray dark-field computed tomography," Phys. Med. Biol. **55**, 5529–5539 (2010).
[49]A. Malecki, G. Potdevin, and F. Pfeiffer, "Quantitative wave-optical numerical analysis of the dark-field signal in grating-based x-ray interferometry," Europhys. Lett. **99**, 48001 (2012).
[50]T. P. Millard, M. Endrizzi, L. Rigon, F. Arfelli, R. H. Menk, J. Owen, E. Stride, and A. Olivo, "Quantification of microbubble concentration through x-ray phase contrast imaging," Appl. Phys. Lett. **103**, 114105 (2013).

[51]M. Strobl, "General solution for quantitative dark-field contrast imaging with grating interferometers," Sci. Rep. **4**, 7243 (2014).
[52]P. Modregger, M. Kagias, S. C. Irvine, R. Brönnimann, K. Jefimovs, M. Endrizzi, and A. Olivo, "Interpretation and utility of the moments of small-angle x-ray scattering distributions," Phys. Rev. Lett. **118**, 265501 (2017).
[53]J. P. Wilde and L. Hesselink, "Statistical optics modeling of dark-field scattering in x-ray grating interferometers: Part 1. Theory," Opt. Express **29**, 40891–40916 (2021).
[54]J. P. Wilde and L. Hesselink, "Statistical optics modeling of dark-field scattering in x-ray grating interferometers: Part 2. Simulation," Opt. Express **29**, 40917–40933 (2021).
[55]S. Meyer, S. Z. Shi, N. Shapira, A. D. A. Maidment, and P. B. Noël, "Quantitative analysis of speckle-based x-ray dark-field imaging using numerical wave-optics simulations," Sci. Rep. **11**, 16113 (2021).
[56]Y. Y. How, D. M. Paganin, and K. S. Morgan, "On the quantification of sample microstructure using single-exposure x-ray dark-field imaging via a single-grid setup," Sci. Rep. **13**, 11001 (2023).
[57]K. Taphorn, L. Kaster, T. Sellerer, A. Hötger, and J. Herzen, "Spectral x-ray dark-field signal characterization from dual-energy projection phase-stepping data with a Talbot-Lau interferometer," Sci. Rep. **13**, 767 (2023).
[58]R. M. Auenhammer, J. Kim, C. Oddy, L. P. Mikkelsen, F. Marone, M. Stampanoni, and L. E. Asp, "X-ray scattering tensor tomography based finite element modelling of heterogeneous materials," npj Comput. Mater. **10**, 50 (2024).
[59]F. Scattarella, S. Tangaro, P. Modregger, M. Stampanoni, L. De Caro, and R. Bellotti, "Post-detection analysis for grating-based ultra-small angle x-ray scattering," Phys. Med. **29**, 478–486 (2013).
[60]N. Francken, J. Sanctorum, J. Renders, P. Paramonov, J. Sijbers, and J. De Beenhouwer, "A condensed history approach to x-ray dark field effects in edge illumination phase contrast simulations," in *2023 45th Annual International Conference of the IEEE Engineering in Medicine & Biology Society (EMBC)* (IEEE, 2023), pp. 1–4.
[61]Y. Sharma, F. Schaff, M. Wieczorek, F. Pfeiffer, and T. Lasser, "Design of acquisition schemes and setup geometry for anisotropic x-ray dark-field tomography (AXDT)," Sci. Rep. **7**, 3195 (2017).
[62]B. Huyge, J. Sanctorum, B. Jeurissen, J. De Beenhouwer, and J. Sijbers, "Fiber orientation estimation from x-ray dark field images of fiber reinforced polymers using constrained spherical deconvolution," Polymers **15**, 2887 (2023).
[63]S. Peter, P. Modregger, M. Fix, W. Volken, D. Frei, P. Manser, and M. Stampanoni, "Combining Monte Carlo methods with coherent wave optics for the simulation of phase-sensitive x-ray imaging," J. Synchrotron. Radiat. **21**, 613–622 (2014).
[64]S. Cipiccia, F. Vittoria, M. Weikum, A. Olivo, and D. Jaroszynski, "Inclusion of coherence in Monte Carlo models for simulation of x-ray phase contrast imaging," Opt. Express **22**, 23480–23488 (2014).
[65]J. Sanctorum, J. Sijbers, and J. De Beenhouwer, "Virtual grating approach for Monte Carlo simulations of edge illumination-based x-ray phase contrast imaging," Opt. Express **30**, 38695–38708 (2022).
[66]J. Sanctorum, J. De Beenhouwer, and J. Sijbers, "X-ray phase contrast simulation for grating-based interferometry using GATE," Opt. Express **28**, 33390–33412 (2020).
[67]P. C. Diemoz, M. Endrizzi, C. E. Zapata, Z. D. Pešić, C. Rau, A. Bravin, I. K. Robinson, and A. Olivo, "X-ray phase-contrast imaging with nanoradian angular resolution," Phys. Rev. Lett. **110**, 138105 (2013).
[68]C. J. Maughan Jones, F. A. Vittoria, A. Olivo, M. Endrizzi, and P. R. T. Munro, "Retrieval of weak x-ray scattering using edge illumination," Opt. Lett. **43**, 3874–3877 (2018).
[69]A. J. den Dekker, J. Gonnissen, A. De Backer, J. Sijbers, and S. Van Aert, "Estimation of unknown structure parameters from high-resolution (S)TEM images: What are the limits?" Ultramicroscopy **134**, 34–43 (2013).
[70]G. Santin, D. Strul, D. Lazaro, L. Simon, M. Krieguer, M. Martins, V. Breton, and C. Morel, "GATE: A Geant4-based simulation platform for PET and SPECT integrating movement and time management," IEEE Trans. Nucl. Sci. **50**, 1516–1521 (2003).
[71]S. Jan, D. Benoit, E. Becheva, T. Carlier, F. Cassol, P. Descourt, T. Frisson, L. Grevillot, L. Guigues, L. Maigne, C. Morel, Y. Perrot, N. Rehfeld, D. Sarrut, D. Schaart, S. Stute, U. Pietrzyk, D. Visvikis, N. Zahra, and I. Buvat, "GATE V6: A major enhancement of the GATE simulation platform enabling modelling of CT and radiotherapy," Phys. Med. Biol. **56**, 881–901 (2011).
[72]S. Agostinelli, J. Allison, K. Amako, J. Apostolakis, H. Araujo, P. Arce, M. Asai, D. Axen, S. Banerjee, G. Barrand, F. Behner, L. Bellagamba, J. Boudreau, L. Broglia, A. Brunengo, H. Burkhardt, S. Chauvie, J. Chuma, R. Chytracek, G. Cooperman, G. Cosmo, P. Degtyarenko, A. Dell'Acqua, G. Depaola, D. Dietrich, R. Enami, A. Feliciello, C. Ferguson, H. Fesefeldt, G. Folger, F. Foppiano, A. Forti, S. Garelli, S. Giani, R. Giannitrapani, D. Gibin, J. J. Gomez Cadenas, I. Gonzalez, G. Gracia Abril, G. Greeniaus, W. Greiner, V. Grichine, A. Grossheim, S. Guatelli, P. Gumplinger, R. Hamatsu, K. Hashimoto, H. Hasui, A. Heikkinen, A. Howard, V. Ivanchenko, A. Johnson, F. W. Jones, J. Kallenbach, N. Kanaya, M. Kawabata, Y. Kawabata, M. Kawaguti, S. Kelner, P. Kent, A. Kimura, T. Kodama, R. Kokoulin, M. Kossov, H. Kurashige, E. Lamanna, T. Lampen, V. Lara, V. Lefebure, F. Lei, M. Liendl, W. Lockman, F. Longo, S. Magni, M. Maire, E. Medernach, K. Minamimoto, P. Mora de Freitas, Y. Morita, K. Murakami, M. Nagamatu, R. Nartallo, P. Nieminen, T. Nishimura, K. Ohtsubo, M. Okamura, S. O'Neale, Y. Oohata, K. Paech, J. Perl, A. Pfeiffer, M. G. Pia, F. Ranjard, A. Rybin, S. Sadilov, E. di Salvo, G. Santin, T. Sasaki, N. Savvas, Y. Sawada, S. Scherer, S. Sei, V. Sirotenko, D. Smith, N. Starkov, H. Stoecker, J. Sulkimo, M. Takahata, S. Tanaka, E. Tcherniaev, E. Safai Tehrani, M. Tropeano, P. Truscott, H. Uno, L. Urban, P. Urban, M. Verderi, A. Walkden, W. Wander, H. Weber, J. P. Wellisch, T. Wenaus, D. C. Williams, D. Wright, T. Yamada, H. Yoshida, and D. Zschiesche, "GEANT4—A simulation toolkit," Nucl. Instrum. Methods Phys. Res., Sect. A **506**, 250–303 (2003).
[73]R. Brun and F. Rademakers, "ROOT—An object oriented data analysis framework," Nucl. Instrum. Methods Phys. Res., Ser. A **389**, 81–86 (1997).
[74]D. M. Paganin and D. Pelliccia, "X-ray phase-contrast imaging: A broad overview of some fundamentals," in *Advances in Imaging and Electron Physics*, edited by M. Hÿtch and P. W. Hawkes (Elsevier, 2021), Chap. 2, Vol. 218, pp. 63–158.
[75]P. R. T. Munro, K. Ignatyev, R. D. Speller, and A. Olivo, "The relationship between wave and geometrical optics models of coded aperture type x-ray phase contrast imaging systems," Opt. Express **18**, 4103–4117 (2010).
[76]P. R. T. Munro, K. Ignatyev, R. D. Speller, and A. Olivo, "Limitations imposed by specimen phase gradients on the design of grating based x-ray phase contrast imaging systems," Appl. Opt. **49**, 3860–3863 (2010).
[77]E. Nazemi, N. Six, D. Iuso, B. De Samber, J. Sijbers, and J. De Beenhouwer, "Monte-Carlo-based estimation of the x-ray energy spectrum for CT artifact reduction," Appl. Sci. **11**, 3145 (2021).
[78]D. Shoukroun, L. Massimi, M. Endrizzi, A. Nesbitt, D. Bate, P. Fromme, and A. Olivo, "Quantification of porosity in composite plates using planar x-ray phase contrast imaging," NDT & E Int. **139**, 102935 (2023).
[79]M. Esposito, I. Buchanan, L. Massimi, J. D. Ferrara, P. R. Shearing, A. Olivo, and M. Endrizzi, "Laboratory-based x-ray dark-field microscopy," Phys. Rev. Appl. **20**, 064039 (2023).
[80]J. B. Keller, "Geometrical theory of diffraction," J. Opt. Soc. Am. **52**, 116 (1962).